Effect of Buffer Layer Structure on the Structural Properties of GaAs Epitaxial Layers Grown on GaP Substrates

Mitsuru Imaizumi[1], Masumi Hirotani[2], Tetsuo Soga[3], and Masayoshi Umeno[3,4]

1 Japan Aerospace Exploration Agency (JAXA), Tsukuba, Ibaraki 305-8505, Japan
E-mail: imaizumi.mitsuru@jaxa.jp

2 Daido Steel Co., Ltd., Minami, Nagoya 457-8545, Japan

3 Nagoya Institute of Technology, Showa, Nagoya 466-8555, Japan

4 C's Techno Inc., Moriyama, Nagoya 463-0003, Japan

Abstract

Three-μm-thick GaAs layers were grown on 2°-off (100) GaP substrates by employing various buffer layer structures, which consist of GaAsP- and InGaAs-based ternary compound semiconductors. To confirm the effects, we altered the layer thickness, the interface lattice mismatch, and number of the layers in the buffer layer structure, and also a superlattice structure was employed in some of the buffer layers. The lattice constants of the layers were controlled by changing the As/P and In/Ga compound ratios. The crystal properties of the grown GaAs layers were characterized with X-ray diffraction, photoluminescence, and etch pit density observations. The effect of the buffer layer structure on the crystallographic character of the GaAs layers was analyzed by introducing a parameter that is a function of the thickness and interface lattice mismatch of each layer in the buffer layer structure. The results suggest that the GaAs layer is relatively relaxed but contains a greater number of dislocations for smaller layer thicknesses and greater lattice mismatches in the buffer layer structure, while the GaAs layer has a smaller number of dislocations but a rather deformed lattice structure for larger layer thicknesses and smaller lattice mismatches. Our parameter is useful for developing design principles of buffer layer structures.

Keywords:

B2. Semiconducting III-V materials; A3. Metalorganic vapor phase epitaxy; A3. Heteroepitaxial growth; B3. Solar cells.

Introduction

In the 1980's, intensive studies on the growth of GaAs or other III–V compound semiconductor materials on silicon (Si) substrates have been performed [1–5]. One of the targets of these studies was realization of low-cost and high-efficiency photovoltaic devices with multi-junction structures based on III–V materials and Si. Several implementations of GaAs solar cells on Si substrates have been reported [6,7], and a reasonable efficiency of ≈ 16% has been attained by Yamaguchi et al. [8]. In addition, the actual operation of the GaAs/Si single-junction solar cells developed by Yamaguchi's group has been demonstrated in space on the satellite ETS-VI launched in 1994 by the National Space Development Agency of Japan (NASDA), which is the former Japan Aerospace Exploration Agency (JAXA) [9]. Other electrical and optical devices using GaAs or related III–V materials have also been demonstrated on Si substrates [10–12]. In this previous research generation, a low-temperature grown thin GaAs layer was mainly employed for the nucleation layer on the Si substrate surface [13].

Recently, the epitaxial growth of III–V compound material layers on Si substrates has again become the focus of interest in terms of cost reduction of high-efficiency multi-junction solar cells [14–18]. In addition, the present high-efficiency triple-junction (3J) solar cells generally utilize Ge wafers for the substrate, but the density of Ge (5.33 g/cm^3) is more than twice that of Si (2.33 g/cm^3). Therefore, replacing Ge with Si substrates would enable us to significantly reduce the weight of the 3J solar cells, which is especially important for space applications. Furthermore, to achieve the highest possible efficiency, the bandgap (Eg) of the Ge bottom subcell (Eg ≈ 0.7 eV) is not wide enough for the combination with those of the InGaP top subcell (Eg ≈ 1.9 eV) and the GaAs middle subcell (Eg ≈ 1.4 eV) in the 3J solar cells. The Eg of Si (≈ 1.1 eV) is preferable also in terms of the solar cell performance. In the present research generation, a thin GaP layer is frequently adopted for the nucleation layer [14–16].

It is well known that it is difficult to grow GaAs layers with high quality on Si substrates. Major issues are (a) the lattice mismatch of about 4 %, and (b) the required polar crystal growth on a non-polar crystal substrate. The first issue causes a high density of misfit dislocations in the GaAs layer, while the second induces anti-phase domains in the layer. As a solution for these issues, we have proposed the utilization of a GaP or an AlP nucleation layer and insertion of strained-layer superlattices (SLSs) [19,20] based on GaAsP alloys for the intermediate buffer layers [4].

Since GaP has a lattice constant at room temperature (0.5451 nm) that is sufficiently matched with that of Si (0.5431 nm), GaP has been considered suitable for the nucleation layer on Si substrates to solve the polar growth issue [21–25]. We have reported a successful growth of GaP layers on Si substrates with noticeable quality [26,27] which can be used as a template layer for GaAs layer epitaxial growth. However, to identify better solutions for the lattice mismatch issue, we have to understand the relation between the crystallographic character of the GaAs layer and the many possible buffer layer structures. The straight-forward characterization of GaAs layers grown on a variety of buffer layers including modified SLS structures has been performed previously [28]. In this study, we extend the simple characterization by an analysis method

that helps us to develop a design principle for a good buffer layer structure and consequently improve the performance of III–V compound devices on Si substrates. For this, we introduce a parameter called "G factor" that characterizes the buffer layer structure and discuss the relation between the crystallographic character of the GaAs layers and the buffer layer structures.

Experimental

As substrates, single crystal GaP wafers with surface orientation (001) ≈ 2º off towards [110] were used. Ten different types of intermediate layer structures were employed to prepare 3.0-μm thick GaAs layers on the GaP substrates (GaAs/GaP). The intermediate buffer layer structures were designed with different lattice constants and thicknesses. The ternary compound semiconductors $GaAs_yP_{1-y}$ and $In_xGa_{1-x}As$ were utilized for the buffer layer materials, because they provide lattice constants between that of GaP and GaAs and above that of GaAs, respectively. Their lattice constants were modified by changing the compound ratios As/P and In/Ga. The ten different intermediate buffer layer structures are described in Table I, and the profiles of their lattice constants and layer thicknesses are schematically presented in Fig. 1 [28].

The structure A is a direct growth without any buffer layer and used as reference. The structures B, C, and E through J except G employ SLSs wherein each layer thickness is less than the critical thickness for formation of misfit dislocations [19,20]. Such a SLS is known to redirect misfit dislocations from the growth direction to the in-plane (lateral) direction, which is beneficial for the GaAs layer quality since the density of threading dislocations in the GaAs layer should be reduced. To confirm this effect, we used structure G where the layer thickness of each layer in the superlattice structure is exceeding the critical thickness. Another considerable method to reduce dislocations in the top GaAs layer is to introduce step-graded buffer layers, which were employed in structures D and L. In terms of the total thickness of the intermediate buffer layers, structure B is the thinnest (40 nm), and C and D are intermediate (0.2 μm). The other buffer layer structures have a thickness of 0.5 μm.

The GaAs/GaP samples explained above were grown by an atmospheric-pressure metal–organic vapor phase epitaxy (MOVPE) apparatus with a horizontal quartz reactor which configuration is schematically illustrated in the left of Fig. 2. Prior to the MOVPE growth, the GaP wafers were cut into two parts and the round side edges were removed (see Fig. 2 center), and each one was used as a substrate for the growth. The GaP substrates were degreased by organic solvents, then etched with a $H_2SO_4+H_2O_2+H_2O$ solution, and finally rinsed with deionized water. The growth was performed on a quartz tray without substrate rotation, and thus there was an epitaxial-layer thickness distribution along the flow direction (the top region was 5-10 percent thicker than the tail region on the substrate). After the growth, the surface morphology of all GaAs layers was mirror-like with a slight cross-hatch pattern, which indicates that the epitaxial growth was successful.

For the analysis of the GaAs layer properties such as orientation, crystallinity, and residual strain, we measured the double-crystal X-ray diffraction (XRD) rocking curves, low-temperature photoluminescence

(PL) spectra, and the etch-pit density (EPD) [28]. The XRD rocking curves were taken for two directions, normal and parallel to the off-angle direction of the GaP substrate. Both the cases the diffraction peak of GaP substrate was searched first and set the angle null (0 arc sec), and then a diffraction spectrum of GaAs layer was acquired. For the low-temperature PL measurements at a temperature of ≈ 4.2 K, the samples were immersed in liquid helium. Low-temperature PL is suitable for analysis of crystal quality in contrast with one at room temperature (RT). In addition, we detected no PL at RT presumably due to low carrier concentration since the GaAs layers were not doped. The EPDs were obtained by etching the sample surfaces via immersion in molten potassium hydroxide (KOH) at ≈ 320 °C for about 30 s. The density of threading dislocations in the GaAs layer can be estimated from the EPD. To avoid the influence of the layer thickness distribution on characterization results, the grown substrates were cleaved exactly in the same manner so that the samples for XRD, PL, EPD and transmission electron microscope (TEM) images were taken from the same position on the substrate as indicated in the right of Fig. 2.

Results

Before we proceed with the analyses of the experimental results, we introduce a parameter that describes the abruptness of a change in the lattice constant with regard to the layer thickness for each layer in the buffer layer structure. We call it "G factor" and define it with

$$\mathrm{G}=\sum \frac{t}{\Delta a} \times 10 \qquad (1)$$

where the sum runs over all layers in the stacked buffer layer structure, t represents the thickness of a single layer in the buffer layer structure, and Δa is the lattice mismatch between this single layer and the layer immediately below. Therefore, the G factor is smaller for a buffer layer structure that consists of thinner layers with greater lattice mismatches. In other words, the G factor becomes large when the change in lattice constant in the buffer layer structure is gradual. The G factors of the GaAs/GaP samples are indicated in parentheses in Fig. 1. In the case of structure A, the G factor is 0 because t = 0. The structure L has the largest G factor (5.56).

A. X-ray diffraction

Here, the relation between the XRD data and the G factor is analyzed. The angular distances between the diffraction peaks of the GaAs layers and the peak of the completely relaxed GaAs ($\Delta\theta_{peak}$) was obtained as illustrated in Fig. 3. The original distance of diffraction peaks between GaAs and GaP is 5040 arc seconds according to their lattice constants. The open circles in Figs. 4 (a) and (b) present the full width at half-maximum (FWHM) of the XRD peaks of the GaAs epitaxial layers measured normal and parallel to the off-cut direction of the GaP substrate, respectively. From both Figs. 4 (a) and (b) it can be confirmed that the

FWHM increases for larger G factors. On the other hand, the dependence of $\Delta\theta_{peak}$ on the G factor is different; we observe an increase of $\Delta\theta_{peak}$ for larger G factors in the parallel direction, but it is constant for the normal direction

B. Photoluminescence

The reference PL spectrum of a homoepitaxial GaAs layer grown by the MOVPE reactor is posted in Fig. 5. For the analysis the highest peak in the exciton-related PL spectrum was selected, and the FWHM of the peak was obtained after peak deconvolution. The PL spectra from the GaAs/GaP samples were analyzed in the same manner, and they showed redshift compared to the PL of the homoepitaxial GaAs. The PL spectra provide information about the crystal quality, and their relation with G factor is shown in Fig. 6. The FWHM of the PL peaks obtained from the GaAs epitaxial layers and the redshift of these peaks ($\Delta\lambda_{peak}$) relative to the free-exciton PL peak of the strain-free GaAs are shown with the closed triangles and open squares, respectively. Figure 6 evidences that the PL FWHM increases for larger G factors. However, it seems that $\Delta\lambda_{peak}$ does not depend on the G factor. It should be mentioned that the PL peak intensities of the GaAs layers grown on the GaP substrate showed also no dependence on the G factor, i.e., all PL peak intensities were about two orders of magnitude smaller than that of the homoepitaxial GaAs layer.

C. Etch-pit density

Figure 7 presents the EPD of the GaAs layers as a function of the G factor. The EPD of structure A (G factor = 0), which is a direct growth without any buffer layer, is the largest among these GaAs/GaP samples. The insertion of an intermediate buffer layer reduces the EPD by about 50%, but the EPDs are almost the same for all buffer structures except structure L (G factor = 5.56). The lowest EPD was obtained for structure L, with an EPD that is less than a fifth of that of structure A.

Discussion

When the lattice constant of the GaAs layer in the growth direction is different from the original value (that is, the lattice constant of the fully relaxed GaAs, 0.5653 nm), the XRD peak of the GaAs layer shifts from the original diffraction position, which is at an angle of 5040 arc sec relative to the GaP diffraction peak. In addition, such a shift will also occur when the lattice plane of the GaAs epitaxial layer is inclined to that of the GaP substrate. Therefore, the angular distance from the original position, $\Delta\theta_{peak}$, should represent the residual strain and/or the misorientation in the GaAs layer. Figure 4 (a) evidenced that the $\Delta\theta_{peak}$ measured along the direction normal to the substrate off-cut direction (hereafter referred to as $\Delta\theta_{peak}^{\perp}$) is almost independent on the G factor, while Fig. 4 (b) showed that the $\Delta\theta_{peak}$ for the parallel direction ($\Delta\theta_{peak}^{/\!/}$) increases with the G factor. However, since both results are obtained from the same lattice plane, the lattice constant of the GaAs layer in the growth direction is the same. Since $\Delta\theta_{peak}^{\perp}$ is almost constant 700 arc sec, this value should

correspond to the lattice constant in the growth direction. When we assume that the misorientation is zero, the lattice constant derived from this $\Delta\theta_{peak}$ is ≈ 0.5623 nm. On the other hand, the PL peak shift from the original wavelength, which is 817 nm (1.517 eV), should reflect the average bandgap shift due to lattice deformation, or strain. In Fig. 6, the PL peak shift, $\Delta\lambda_{peak}$, is almost independent of the G factor. The correlation between $\Delta\theta_{peak}^{//}$ and $\Delta\lambda_{peak}$ as well as that between $\Delta\theta_{peak}^{//}$ and EPD is shown in Fig. 8. It is evident that $\Delta\lambda_{peak}$ is also independent of $\Delta\theta_{peak}^{//}$. This fact supports the above assignment of the lattice constant along the growth direction. Thus, $\Delta\theta_{peak}^{//}$, which changes from ~700 to ~2300 arc sec for G factors between 0 and 6, is considered to indicate a change in the misorientation with respect to the surface lattice plane of the GaP substrate, and this misorientation becomes larger when the G factor increases. According to Fig. 8, the EPD, or the density of dislocations in the GaAs layer due to the misfit, decreases as the misorientation increases.

The FWHM of the XRD peak, $FWHM_{XRD}$, represents the dislocation density and/or the residual strain in a crystal. Figure 4 shows that the $FWHM_{XRD}$ for both directions, i.e., normal and parallel to the GaP substrate off-cut direction, increases as the G factor increases. Figure 9 plots the correlation between the average $FWHM_{XRD}$ and the FWHM obtained from the PL peak, $FWHM_{PL}$, as well as that between the average $FWHM_{XRD}$ and EPD. We confirm a negative correlation for the latter. Therefore, we consider that $FWHM_{XRD}$ cannot represent the dislocation density in this case. The $FWHM_{PL}$ should reflect the energy gap dispersion due to the crystal's lattice distortion, which corresponds to the residual strain in the GaAs layer. Since $FWHM_{XRD}$ and $FWHM_{PL}$ have a positive correlation as indicated in Fig. 9, $FWHM_{XRD}$ should reflect the residual strain. However, as discussed above, the lattice constant of the GaAs layer in growth direction is supposed to be same for all structures. Hence, $FWHM_{XRD}$ must indicate the lattice distortion in the growth direction. On the other hand, the negative correlation between $FWHM_{XRD}$ and EPD implies that the residual strain in the GaAs layers is reduced when the dislocation density is high.

It is very interesting to note that, according to the very similar EPDs around G = 2.8 in Fig. 7, the insertion of SLSs into the buffer layer structures does not seem to reduce the dislocation density as expected [29]. The cross-sectional transmission electron microscope (TEM) images of some buffer layers are provided in Fig. 10. Figures 10 (a), (b), and (c) correspond to structures C, K (with SLSs) and L (no SLS), respectively. Although the layer thicknesses in the SLSs in structures C and K were designed to be less than the critical thickness, the TEM images indicate that a three-dimensional growth occurred and consequently the expected buffer layer structures were not attained. This might be one of the reasons why the SLS structure was not able to reduce the dislocation density in this work. On the other hand, a planar growth was most likely achieved in the step-graded structure L whose G factor is the largest (5.56) among the structures used in this work. This is probably the reason why structure L exhibited the lowest dislocation density as well as the largest residual strain.

Summary

GaAs layers with different crystal properties were epitaxially grown on GaP substrates by MOVPE utilizing various buffer layer structures. To identify the effects of buffer layer structure, we altered both the thickness and interface lattice mismatch in the buffer layers, and employed SLS structures. The GaAs layers were characterized by XRD, low-temperature PL, and EPD measurements. To analyze the rather complex effects of the buffer layer structures on the crystallographic character of the GaAs layers, we proposed a new parameter that helps us to identify the design principles of appropriate buffer layer structures. The experimental results suggested that the GaAs layer is relatively relaxed but contains a greater number of dislocations when smaller layer thicknesses and larger lattice mismatches are introduced in the buffer layer structure. On the other hand, the GaAs layer has a smaller number of dislocations but a rather deformed lattice structure when the buffer layer design is opposite. In addition, in the case of small layer thicknesses and large lattice mismatches, the GaAs lattice plane tends to grow with an inclination towards the off-cut angle direction of the GaP substrate. Furthermore, the inserted SLSs did not work as expected because of a deformation of the layer structure during growth.

Acknowledgement

The authors would like to thank Prof. T. Saka (Daido Institute of Technology) and Dr. T. Kato (Daido Steel Co. Ltd.) for the fruitful discussions and their suggestions.

References

[1] M. Akiyama, Y. Kawarada, K. Kaminishi, Growth of GaAs on Si by MOVCD, J. Cryst. Growth 68 (1984) 21-26.

[2] W.I. Wang, Molecular beam epitaxial growth and material properties of GaAs and AlGaAs on Si (100), Appl. Phys. Lett. 44 (1984) 1149-1151

[3] B.-Y. Tsaur, G.M. Metze, Molecular beam epitaxy of GaAs and AlGaAs on Si, Appl. Phys. Lett. 45 (1984) 535-536.

[4] T. Soga, S. Hattori, S. Sakai, M. Takeyasu, M. Umeno, Characterization of epitaxially grown GaAs on Si substrates with III‐V compounds intermediate layers by metalorganic chemical vapor deposition, J. Appl. Phys. 57 (1985) 4578-.

[5] H. Horikawa, Y. Kawai, M. Akiyama, M. Sakuta, Heteroepitaxial growth of InP on Si substrates by LP-MOVPE, J. Cryst. Growth, 93 (1988) 523-526.

[6] R.P. Gale, J.C.C. Fan, B.Y. Tsaur, G.W. Turner, F.M. Davis, GaAs Shallow-Homojunction Solar Cells on Ge-Coated Si Substrates, IEEE Electron Device Lett. 2 (1981) 169-171.

[7] M. Yang, T. Soga, T. Egawa, T. Jimbo, M. Umeno, Three-terminal monolithic cascade GaAs/Si solar cells, Sol. Ener. Mat. Sol. Cells 35 (1994) 45-51.

[8] M. Yamaguchi, Y. Ohmachi, T. Oh'hara, Y. Kadota, M. Imaizumi, and S. Matsuda, GaAs solar cells grown on Si substrates for space use, Prog. Photovolt.: Res. Appl. 9 (2001) 191-201.

[9] M. Imaizumi, O. Anzawa, S. Matsuda, M. Yamaguchi, T. Ohara, Flight degradation data of GaAs-on-Si solar cells on highly irradiated ETS-VI, Conf. Record of 28th IEEE Photovolt. Spec. Conf. (2000) 1075-1078.

[10] Y. Shinoda, T. Nishioka, Y. Ohmachi, GaAs Light Emitting Diodes Fabricated on SiO_2/Si Wafers, Jpn. J. Appl. Phys. 22 (1983) L450-L451.

[11] T.H. Windhorn, G.M. Metze, B.-Y. Tsaur, J.C.C. Fan, AlGaAs double-heterostructure diode lasers fabricated on a monolithic GaAs/Si substrate, Appl. Phys. Lett., 45 (1984) 309-311.

[12] G.M., Metze, H.K. Choi, B.-Y. Tsaur, Metal-semiconductor field-effect transistors fabricated in GaAs layers grown directly on Si substrates by molecular beam epitaxy, Appl. Phys. Lett. 45 (1984) 1107-1109.

[13] M. Akiyama, Y. Kawarada, T. Ueda, S. Nishi, K. Kaminishi, Growth of high quality GaAs layers on Si substrates by MOCVD, J. Cryst. Growth, 77 (1986) 490-497.

[14] J.R. Lang, J. Faucher, S. Tomasulo, K.N. Yaung, M.L. Lee, GaAsP solar cells on GaP/Si grown by molecular beam epitaxy, Conf. Record of 39th IEEE Photovoltaic Spec. Conf. (2013) 2100-2104.

[15] T. J. Grassman, J. A. Carlin, B. Galiana, F. Yang, M. J. Mills, S. A. Ringel, MOCVD-Grown GaP/Si Subcells for Integrated III–V/Si Multijunction Photovoltaics, IEEE J. Photovoltaics, 4 (2014) 972-980.

[16] K. Yamane, N. Urakami, H. Sekiguchi, A. Wakahara, III-V-N Compounds for Multi-Junction Solar Cells on Si, Conf. Record of 40th IEEE Photovolt. Spec. Conf. (2014) 2792-2796.

[17] L. Wang, B. Conrad, A. Soeriyadi, M. Diaz, X. Zhao, D. Li, A. Lochtefeld, A. Gerger, C. Ebert, I. Perez-Wurfl, A. Barnett, Current matched GaAsP/SiGe tandem device on Si over 20% efficiency under indoor measurement, Conf. Record of 42nd IEEE Photovolt. Spec. Conf. (2015) 1-4.

[18] R. Cariou, J. Benick, P. Beutel, N. Razek, C. Flötgen, M. Hermle, D. Lackner, S.W. Glunz, A.W. Bett, M. Wimplinger, F. Dimroth, Monolithic Two-Terminal III–V//Si Triple-Junction Solar Cells With 30.2% Efficiency Under 1-Sun AM1.5G, IEEE J. Photovoltaics, 7 (2017) 367-373.

[19] J.W. Matthews, A.E. Blakeslee, Defects in epitaxial multilayers: I. Misfit dislocations, J. Cryst, Growth 27 (1974) 118-125.

[20] G.C. Osbourn, Strained-layer superlattices from lattice mismatched materials, J. Appl. Phys. 53 (1982) 1586-1589.

[21] J.P. Andre, J. Hallas, C. Schiller, Heteroepitaial growth of GaP on silicon, J. Cryst, Growth, 31 (1975) 147-157.

[22] H.B. Pogge, B.M. Kemlage, and R.W. Broadie, The heteroepitaxial growth of GaP films on Si substrates, J. Cryst, Growth, 37 (1977) 13-22.

[23] J.M. Olson, M.M. Al-Jassim, A. Kibbler, and K.M. Jones, MOCVD growth and characterization of GaP on Si, J. Cryst, Growth, 77 (1986) 515-523.

[24] B. Kunerta, I. Némethb, S. Reinhardb, K. Volzb, and W. Stolzb., Si (001) surface preparation for the antiphase domain free heteroepitaxial growth of GaP on Si substrate, Thin Solid Films 517 (2008) 140-143.

[25] K. Yamane, T. Kawai, Y. Furukawa, H. Okada, and A. Wakahara, Growth of low defect density GaP layers on Si substrates within the critical thickness by optimized shutter sequence and post-growth annealing, J. Cryst, Growth 312 (2010) 2179-2184.

[26] T. Soga, Y. Kohama, K. Uchida, M. Tajima, T. Jimbo and M. Umeno, MOCVD growth and characterization of GaAs and GaP grown on Si substrates, J. Cryst, Growth 93 (1988) 499-503.

[27] M. Imaizumi, T. Saka, T. Jimbo, T. Soga and M. Umeno, Two-Dimensional Growth of GaP on Si Substrates under High V/III Ratio by Metal Organic Vapor Phase Epitaxy, Jpn. J Appl. Phys., 30 (1991) 451-453.

[28] M. Imaizumi, M. Hirotani, T. Soga, Study on effect of an intermediate buffer layer structure on the growth of GaAs layers on GaP substrates, Proc. 42nd IEEE Photovoltaic Specialists Conf. (2015), DOI: 10.1109/PVSC. 2015.7356240.

[29] M. Yamaguchi, T. Nishioka and M. Sugo, Analysis of strained-layer superlattice effects on dislocation density reduction in GaAs on Si substrates, Appl. Phys. Lett. 54 (1989) 24-26.

Table and Figure captions

Table I. Stacking structures of the intermediate buffer layers that are inserted between the GaP substrate and the 3-μm-thick GaAs epitaxial layer. The numbers in the parentheses in the structure are the thicknesses of the individual layer.

Fig. 1. Schematic of the thickness and lattice constant profiles of the intermediate buffer layers between the GaP substrate and the 3-μm-thick GaAs epitaxial layer. The numbers in the parentheses below the sample identification letters are the G factors.

Fig. 2. Schematic of the configuration of the MOCVD reactor (left), diagram of 2-inch GaP wafer used in this study (center), and diagram of cleavage of samples for XRD, PL, EPD and TEM characterizations (right).

Fig. 3. Schematic of the XRD diffraction spectrum of GaAs/GaP sample. The peak position of a diffraction spectrum of GaP substrate was set to be 0 arc sec. The $\Delta\theta_{peak}$ and the FWHM of a GaAs layer diffraction peak were determined as illustrated.

Fig. 4. The FWHM of the XRD peaks of the GaAs epitaxial layers measured (a) normal to the off-cut direction and (b) along the off-cut direction are shown with the open circles. The closed diamonds plot the angular distances from the peaks of the GaAs layers towards the peak of the relaxed GaAs crystal ($\Delta\theta_{peak}$).

Fig. 5. The reference PL spectrum of a homoepitaxial GaAs layer grown by the MOVPE reactor. The highest peak in the exciton-related PL spectrum was selected for analysis. FWHM of the peak was obtained after peak deconvolution. The PL spectra of GaAs/GaP samples were analyzed in the same manner.

Fig. 6. The FWHM of the PL peaks obtained from the GaAs epitaxial layers at 4.2 K are shown with the closed triangles. The open squares show the redshift ($\Delta\lambda_{peak}$) of the peaks obtained from the GaAs layers relative to the free-exciton peak of the relaxed GaAs crystal.

Fig. 7. The measured EPDs of the GaAs epitaxial layers as a function of the G factor.

Fig. 8. The correlation between $\Delta\theta_{peak}^{//}$ (obtained from the XRD data parallel to the substrate off-cut direction), and $\Delta\lambda_{peak}$ (obtained from the PL spectra) is shown with the open squares. The correlation between $\Delta\theta_{peak}^{//}$ and the EPD is shown with the closed circles.

Fig. 9. The correlation between the XRD FWHM (average of components obtained for the directions normal and parallel to the substrate off-cut direction) and the PL FWHM is shown with the open squares. The correlation between the XRD FWHM and the EPD is shown with the closed circles.

Fig. 10. Cross-sectional TEM images of several intermediate buffer layers. The upper part is the GaAs epitaxial layer and the lower part is the GaP substrate.

Table I

ID	Sub.	Intermediate buffer layers	GaAs
A	GaP	(none)	GaAs (3.0 μm)
B		$GaP/GaAs_{0.5}P_{0.5}$ (10 nm) ×1 period / $GaAs_{0.5}P_{0.5}$/GaAs (10 nm) ×1 period	
C		$GaP/GaAs_{0.5}P_{0.5}$ (10 nm):SLS1 ×5 periods / $GaAs_{0.5}P_{0.5}$/GaAs (10 nm):SLS2 ×5 periods	
D		$GaAs_{0.2}P_{0.8}$ (0.05 μm) / $GaAs_{0.4}P_{0.6}$ (0.05 μm) / $GaAs_{0.6}P_{0.4}$ (0.05 μm) / $GaAs_{0.8}P_{0.2}$ (0.05 μm)	
E		SLS1 ×5 periods / $GaAs_{0.5}P_{0.5}$ (0.3 μm) / SLS2 ×5 periods	
F		SLS1 ×10 periods / $GaAs_{0.5}P_{0.5}$ (0.1 μm) / SLS2 ×10 periods	
G		$GaP/GaAs_{0.5}P_{0.5}$ (20 nm) ×5 periods / $GaAs_{0.5}P_{0.5}$ (0.1 μm) / $GaAs_{0.5}P_{0.5}$/GaAs (20 nm) ×5 periods	
H		SLS1 ×5 periods / $GaAs_{0.5}P_{0.5}$ (0.1 μm) / SLS2 ×5 periods / GaAs (0.1 μm) / $GaAs/In_{0.17}Ga_{0.83}As$ (10 nm) ×5 periods	
J		SLS1 ×5 periods / SLS2 ×5 periods / GaAs (0.2μm) / $GaAs_{0.8}P_{0.2}/In_{0.08}Ga_{0.92}As$ (10 nm) ×5 periods	
K		$GaP/GaAs_{0.33}P_{0.67}$ (10 nm) ×5 periods / $GaAs_{0.33}P_{0.67}$ (0.1 μm) / $GaAs_{0.33}P_{0.67}$/ $GaAs_{0.67}P_{0.33}$ (10 nm) ×5 periods / $GaAs_{0.67}P_{0.33}$ (0.1 μm) / $GaAs_{0.67}P_{0.33}$/GaAs (10 nm) ×5 periods	
L		$GaAs_{0.2}P_{0.8}$(0.125 μm) / $GaAs_{0.4}P_{0.6}$(0.125 μm) / $GaAs_{0.6}P_{0.8}$(0.125 μm) / $GaAs_{0.8}P_{0.2}$(0.125 μm)	

Figure 1

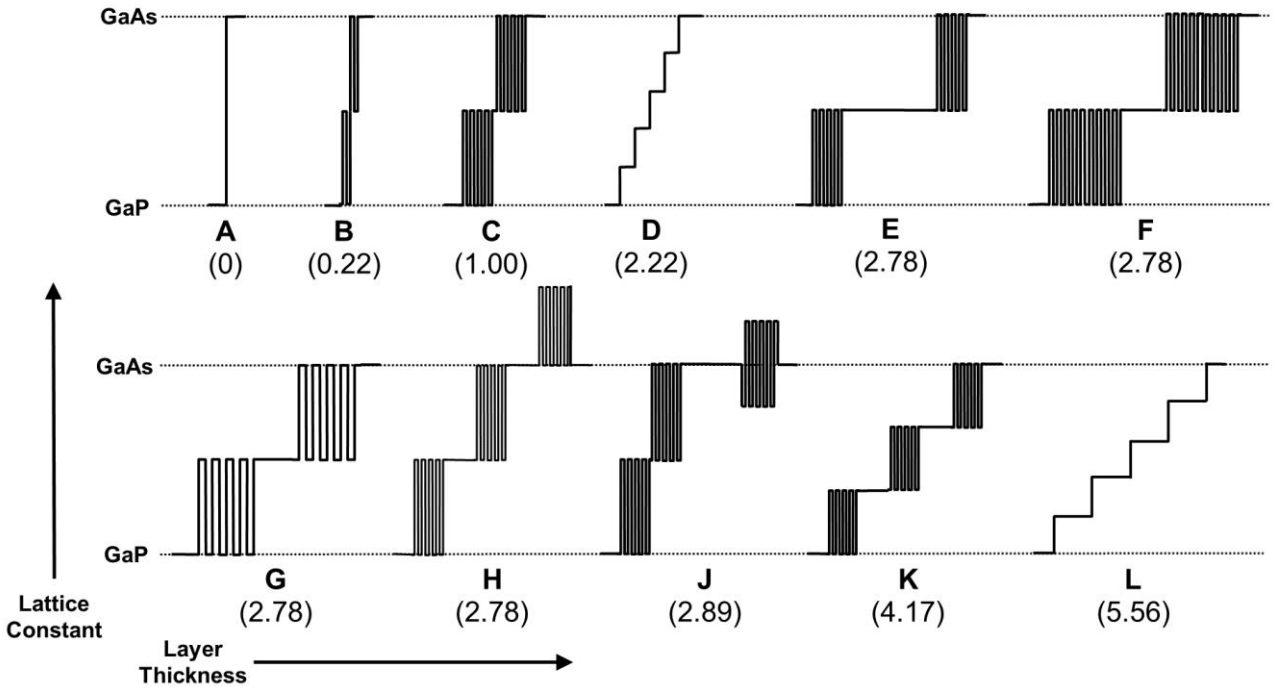
GaAs
GaP
A
(0)
B
(0.22)
C
(1.00)
D
(2.22)
E
(2.78)
F
(2.78)
GaAs
GaP
G
(2.78)
H
(2.78)
J
(2.89)
K
(4.17)
L
(5.56)
Lattice Constant
Layer Thickness

Figure 2

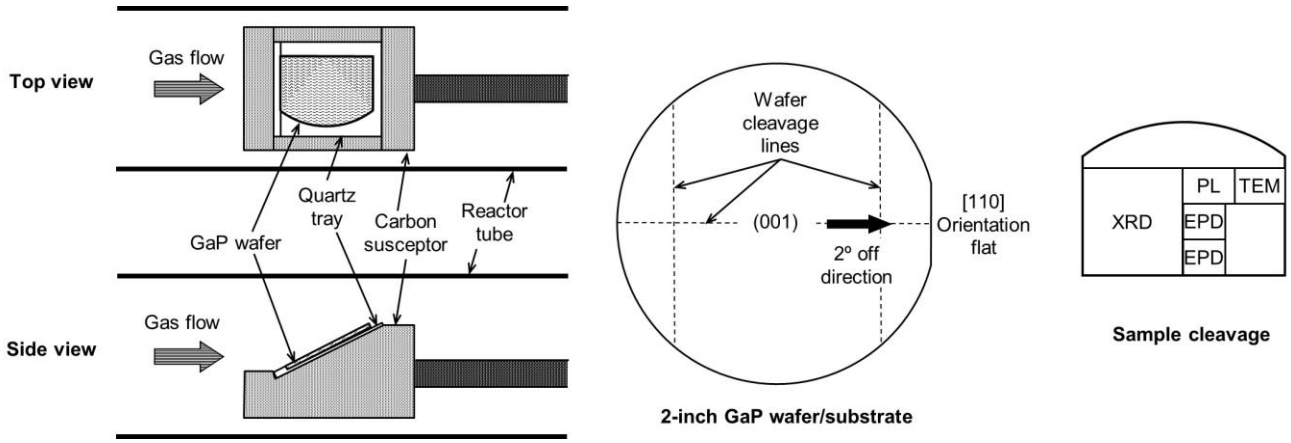
Top view
Gas flow
Quartz tray
Carbon susceptor
Reactor tube
GaP wafer
Side view
Gas flow
Wafer cleavage lines
(001)
2° off direction
[110] Orientation flat
2-inch GaP wafer/substrate
XRD
PL
TEM
EPD
EPD
Sample cleavage

Figure 3

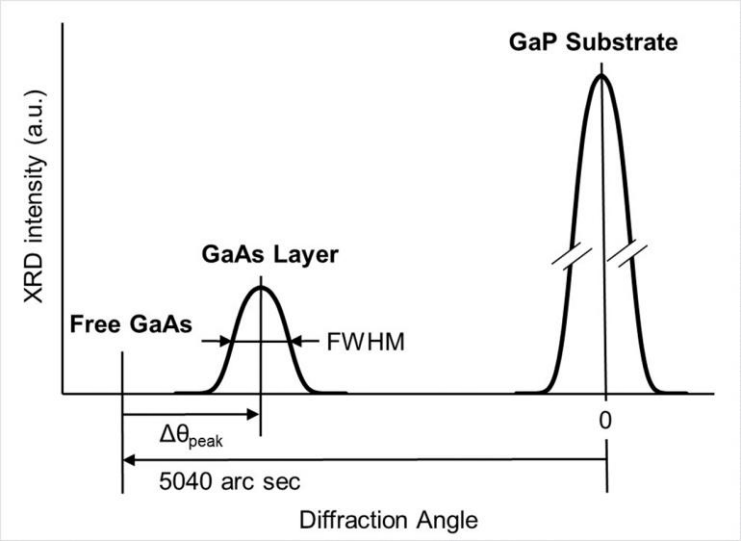
GaP Substrate
XRD intensity (a.u.)
GaAs Layer
Free GaAs
FWHM
$\Delta\theta_{peak}$
0
5040 arc sec
Diffraction Angle

Figure 4

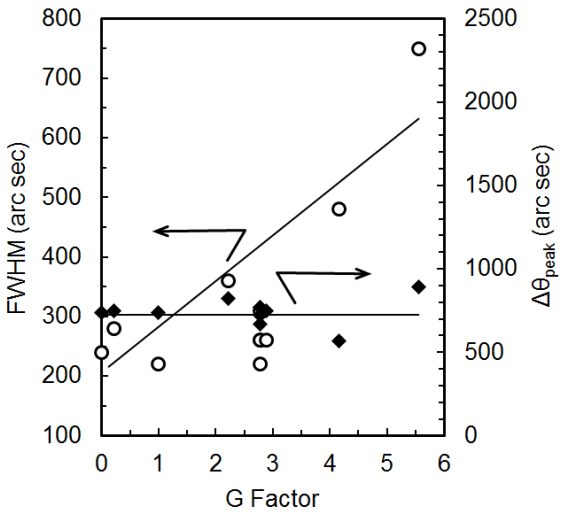

(a) Normal to off-cut direction

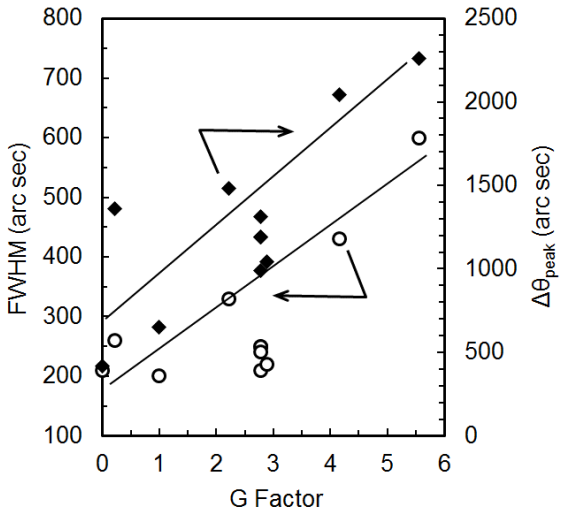

(b) Parallel to off-cut direction

Figure 5

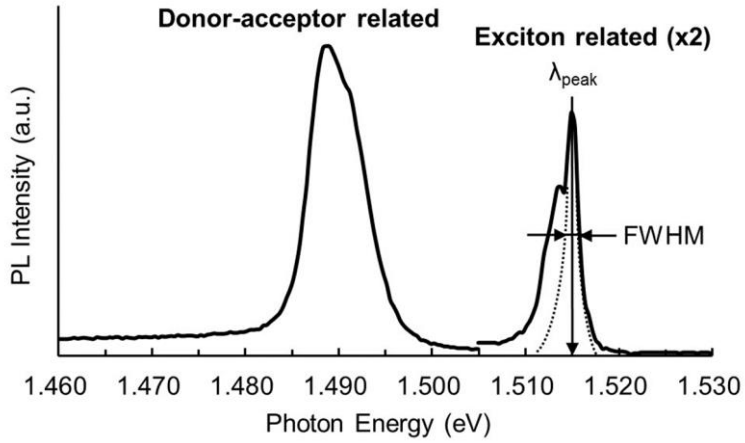
Donor-acceptor related
Exciton related (x2)
λpeak
FWHM
PL Intensity (a.u.)
1.460
1.470
1.480
1.490
1.500
1.510
1.520
1.530
Photon Energy (eV)

Figure 6

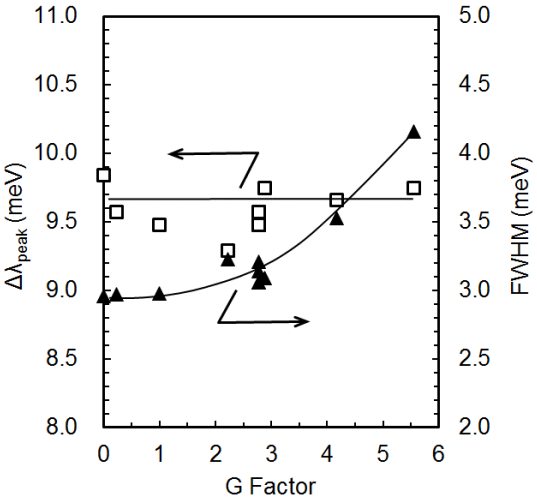
11.0
10.5
10.0
9.5
9.0
8.5
8.0
$\Delta\lambda_{peak}$ (meV)
5.0
4.5
4.0
3.5
3.0
2.5
2.0
FWHM (meV)
0
1
2
3
4
5
6
G Factor

Figure 7

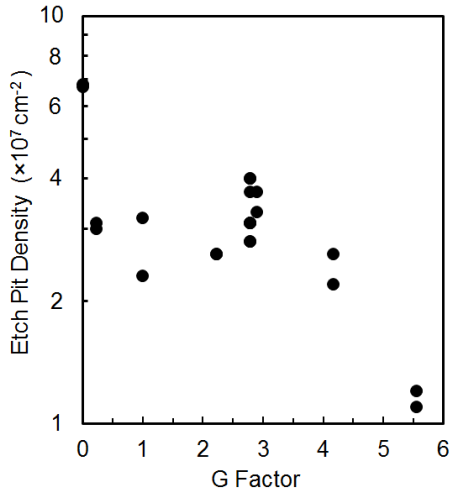

Figure 8

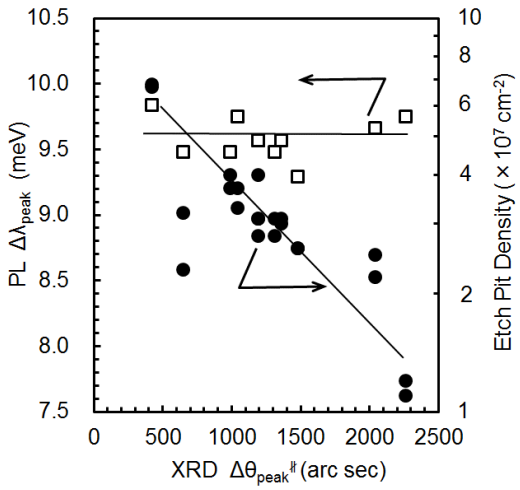
10.5
10.0
9.5
9.0
8.5
8.0
7.5
PL Δλpeak (meV)
0
500
1000
1500
2000
2500
XRD Δθpeak// (arc sec)
10
8
6
4
2
1
Etch Pit Density (× 10⁷ cm⁻²)

Figure 9

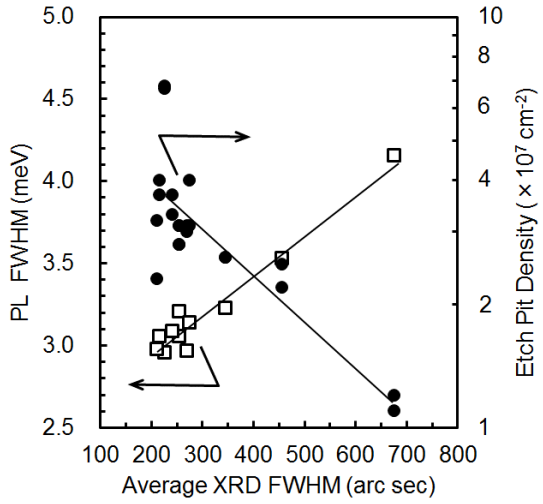
5.0
4.5
4.0
3.5
3.0
2.5
PL FWHM (meV)
10
8
6
4
2
1
Etch Pit Density (x 10⁷ cm⁻²)
100 200 300 400 500 600 700 800
Average XRD FWHM (arc sec)

Figure 10

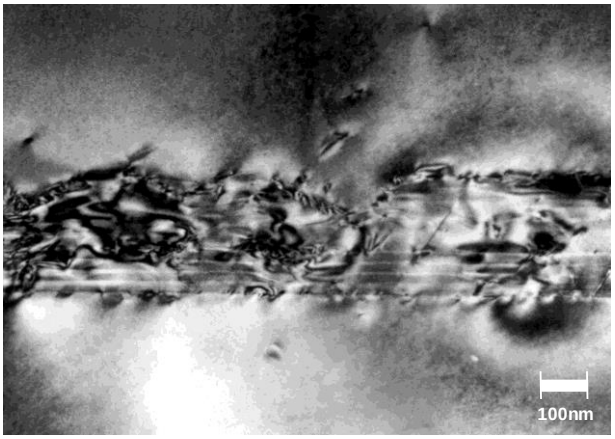

(a) Structure C

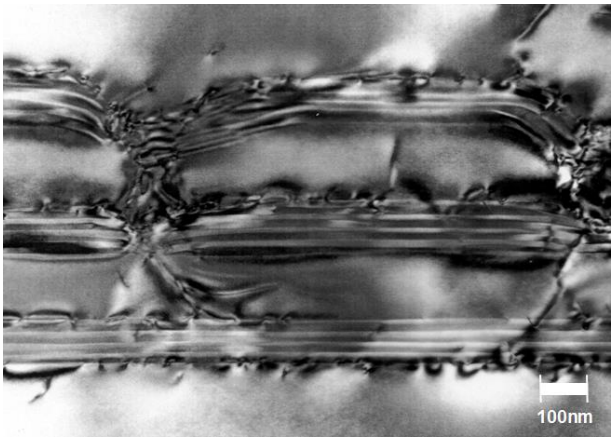

(b) Structure K

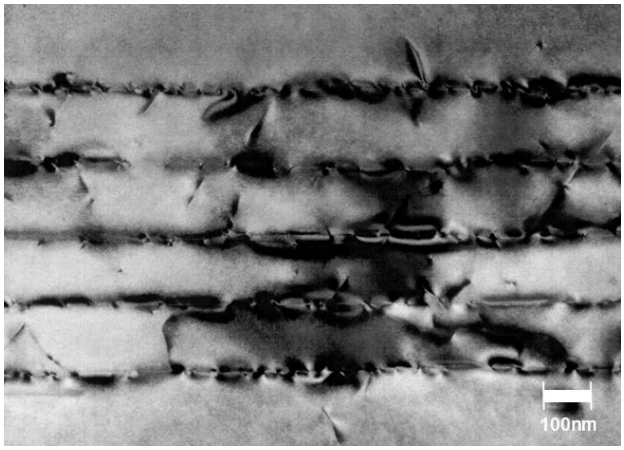

(c) Structure L